Title	Noncontact Operation-State Monitoring Technology Based on Magnetic-Field Sensing for Overhead High-Voltage Transmission Lines
Author(s)	Sun, X; Huang, Q; Hou, Y; Jiang, L; Pong, PWT
Citation	IEEE Transactions on Power Delivery, 2013, v. 28 n. 4, p. 2145-2153
Issued Date	2013
URL	http://hdl.handle.net/10722/185887
Rights	Creative Commons: Attribution 3.0 Hong Kong License

Noncontact Operation-State Monitoring Technology Based on Magnetic-Field Sensing for Overhead High-Voltage Transmission Lines

Xu Sun, Qi Huang, *Senior Member, IEEE*, Yunhe Hou, *Member, IEEE*, Lijun Jiang, *Senior Member, IEEE*, and Philip W. T. Pong, *Senior Member, IEEE*

***Abstract*—This paper proposed a novel noncontact technology of operation-state monitoring based on magnetic-field sensing for high-voltage transmission lines, which can simultaneously measure both electrical and spatial parameters in real time. This technology was derived from research on the magnetic-field distribution at the ground level when the transmission lines operate in different states, including sagging, galloping, and current imbalance. Two typical models of high-voltage three-phase transmission lines were simulated, and the resulting magnetic fields were calculated. The correlation between the magnetic-field variations and the operation states were analyzed. Based on such correlation, a source reconstruction method was developed to reconstruct the spatial and electrical parameters from the magnetic field emanated by the overhead transmission lines. The reconstruction results for the 500-kV and 220-kV transmission lines verify the feasibility and practicality of this novel noncontact transmission-line monitoring technology based on magnetic-field sensing.**

***Index Terms*—Magnetic-field sensing, magnetoresistive sensor, noncontact monitoring, overhead transmission line, smart grid.**

I. Introduction

HIGH-VOLTAGE transmission lines are the most effective way for long-distance power delivery from sources to distribution networks with the maximum ampacity. These days, the planning, operation, and maintenance of the power grid can be improved by employing large-scale wide-area monitoring, protection and control (WAMPAC) applications [1]. Wide-area monitoring requires the operation states of the transmission-line networks to be monitored and reported to the control center in real time. Both the electrical and spatial parameters of the transmission lines should be accurately detected. It drives the development of a real-time operation-state monitoring technology which is able to measure electrical parameters, including amplitude, phase angle, frequency, and waveform of the phase currents. On the other hand, the technology should also be able to obtain spatial parameters, including conductor sagging and galloping of the transmission lines. The technology can be potentially applied in the transmission lines in large scale for finding out the abnormal parameter changes of transmission-line spans in order to enable engineers to accurately and quickly locate the fault. Apart from wide-scale deployment and real-time measurement, a desirable monitoring technology must be stable, safe, easy for installation, and self-reliant so that when very serious faults occur due to unexpected changes of transmission-line parameters, the monitoring system can maintain stability and accuracy in detection. A noncontact monitoring technology is needed to fulfill these requirements. In addition, the noncontact nature avoids installation works on live wires, guaranteeing the safety of installation personnel and reducing maintenance works for them. These objectives motivate the development of a noncontact real-time operation-state monitoring technology for the overhead high-voltage (HV) power transmission line in this paper.

Presently, several techniques and devices are applied in operation-state monitoring for transmission lines. Some of them are designed for detecting the electrical parameters of the transmission lines. For example, current transformers (CTs) are installed in substations and are typically used for current measurement [2], [3]. In practice, it is impossible to equip current transformer (CTs) outside substations due to their large dimensions, weight, and cost. Thus fault location in the large-scale transmission-line networks with accuracy cannot be achieved by using CTs. Other devices are based on various mechanisms to directly or indirectly estimate the spatial parameters of the transmission lines. A temperature measuring system by SMT [4] is installed at the transmission-line span. It calculates the transmission-line sag from the measured temperature. A transmission line monitoring system (CAT-1) is used to monitor the mechanical tension of a transmission-line span at a dead-end structure [5]. It calculates the sags, clearances, and average conductor temperature of the transmission lines from the measured tension. The shortcomings of these two systems are their in-contact operation with the live conductor. Siemens-Milltronics SONAR clearance monitoring equipment [6] is a portable device, and its operation does not require contact with live lines. An operator can use it to measure the clearance of a transmission-line span and calculate the conductor temperature and wind speed. However, the

Manuscript received July 06, 2012; revised January 09, 2013 and March 25, 2013; accepted May 13, 2013. Date of publication August 08, 2013; date of current version September 19, 2013. This work was supported in part by the Seed Funding Program for Basic Research, in part by the Small Project Funding Program, in part by the Seed Funding for Applied Research from the University of Hong Kong, in part by ITF Tier 3 funding (ITS/112/12), and in part by the RGC-GRF Grant (HKU 704911P). Paper no. TPWRD-00707-2012.

X. Sun, Y. Hou, L. Jiang, and P. W. T. Pong are with Department of Electrical and Electronic Engineering, The University of Hong Kong, Hong Kong, China (e-mail: sunxu@eee.hku.hk; yhhou@eee.hku.hk; jianglj@hku.hk; ppong@eee.hku.hk).

Q. Huang is with the School of Energy Science and Engineering, University of Electronic Science and Technology of China, Chengdu 610054, China (e-mail: hwong@uestc.edu.cn).

Color versions of one or more of the figures in this paper are available online at http://ieeexplore.ieee.org.

Digital Object Identifier 10.1109/TPWRD.2013.2264102

Siemens-Milltronics as well as the SMT and CAT-1 suffer the disadvantage that their calculations are based on complicated mathematical models involving many different physical parameters, such as conductor temperature, material coefficients, and wind speed which do not have a direct relation to the conductor current or position. A technology based on differential global positioning system (DGPS) enables the direct measurement of the conductor position [7]. However, since the GPS receiver has to be mounted on the phase conductor, installation on live wire cannot be avoided. Video and image-processing technologies are used to detect spatial parameters of the transmission lines [8]. It requires contact with phase conductors for placing the targets. Under rough weather conditions, such as heavy rain, snow, or dense fog, the resolution of imaging may be impaired due to insufficient ambient light. A sensor platform called "Power Donut" can measure electrical and spatial parameters, including transmission-line current, conductor temperature, and angle of inclination [9]. It requires live-wire installation and operates in-contact with the conductor. Moreover, the "Power Donut" is unable to measure the galloping of the transmission-line conductor. In short, the existing methods suffer disadvantages of contact measurement, installation with live wire, complicated model, high cost, and instability with adverse ambient conditions. Moreover, most of them cannot simultaneously measure the electrical and spatial parameters of the transmission lines.

In this paper, a novel noncontact monitoring technology for high-voltage transmission-line operation-state monitoring is proposed which can overcome the shortcomings of the existing methods. The magnetic-field variation is found to be directly correlated with the electrical and spatial parameters of the line conductors. Based on such correlation, a source reconstruction algorithm is developed for estimating the electrical and spatial parameters from the measured magnetic field. The source reconstruction results can accurately provide electrical and spatial parameters of the transmission line. Typical problems of transmission-line operation states are considered, including conductor sagging, galloping, as well as current imbalance in amplitude and phase angle. This novel noncontact technique does not require installation or operation on live wires. Magnetic-field sensing can be implemented with low-cost and low-energy consumption magnetic sensors. Moreover, this technique is invulnerable to weather conditions since the weather normally does not affect the magnetic field.

II. Magnetic Field of the Transmission Line

The magnetic field from an overhead transmission line can be calculated by the Biot–Savart law in view of the following facts. Although the electric and magnetic fields from overhead transmission lines are coupled, there is no radiation at such a low frequency at 50 or 60 Hz. Thus, the electric and magnetic fields can be treated as decoupled and analyzed separately. The resulting magnetic field in the vicinity of multiconductor power lines can be evaluated by superimposing the contribution from each phase current flowing in the conductors and the image currents introduced in the conducting ground. The conditions of conductor sagging and galloping are involved in the computation. Conductor sagging is length extension of a line conductor

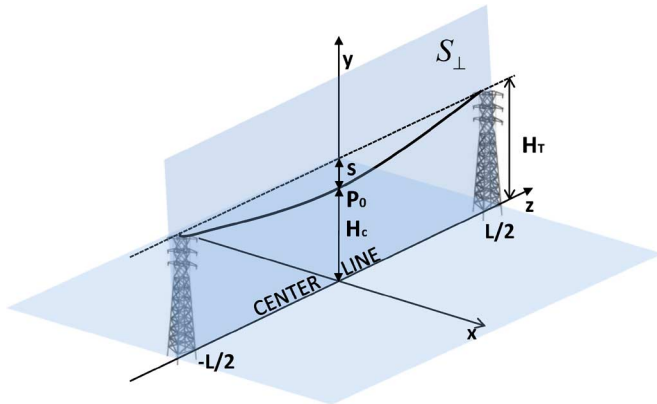

Fig. 1. Profile of the conductor catenary of transmission-line conductor sagging.

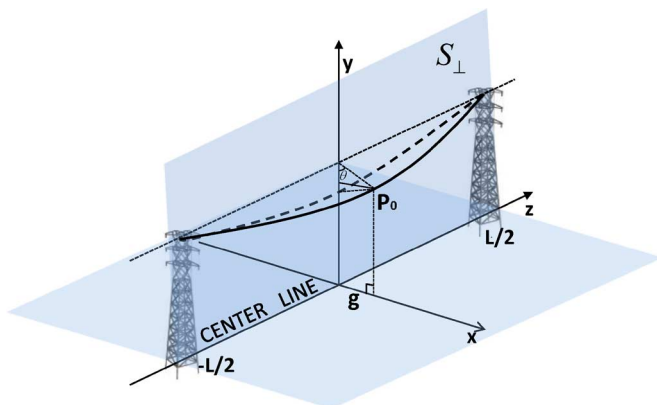

Fig. 2. Profile of the conductor catenary of transmission-line conductor galloping.

which can lower the conductor height. When dealing with the scenario of sagging, the conductors suspended between towers are catenary due to their own weight. The profile of a conductor catenary is shown in Fig. 1: H_T is the height of the catenary endpoints, s is the extent of sag, and H_C is the height of the lowest point P_0 of the catenary. The whole conductor catenary is in the plane $S_\perp$ which is perpendicular to the ground surface. Galloping is a wind-induced large-amplitude oscillation of the line conductors. When taking it into account, as shown in Fig. 2, the conductor catenary departs from $S_\perp$ (except the two endpoints) and rotates θ degree around its horizontal axis along the z-direction which is determined by the two endpoints. The x-direction displacement of the point P_0 indicates the galloping horizontal amplitude g. The sagging and galloping can significantly change the spatial parameters of the transmission-line conductor. They are considered to formulate the function of conductor catenary. The detailed calculation of the magnetic field of the transmission line with sagging and galloping is described in Appendix. Then, the magnetic-field distributions of two typical overhead transmission-line configurations are simulated as shown in Fig. 3. Their line voltages are 500 kV [Fig. 3(a)] and 220 kV [Fig. 3(b)], respectively. They are operated with a current of 1 kA per phase. In order to demonstrate that the emanated magnetic field can provide the information of the operation states, simulations were carried out to show the variation

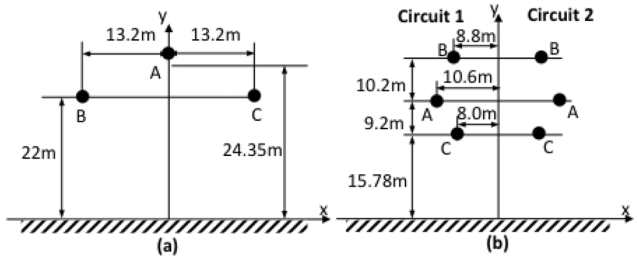

Fig. 3. Two different configurations of the overhead power transmission lines. (a) The line voltage is 500 kV. (b) The line voltage is 220 kV. The phase of each conductor is denoted as "A", "B", and "C", respectively.

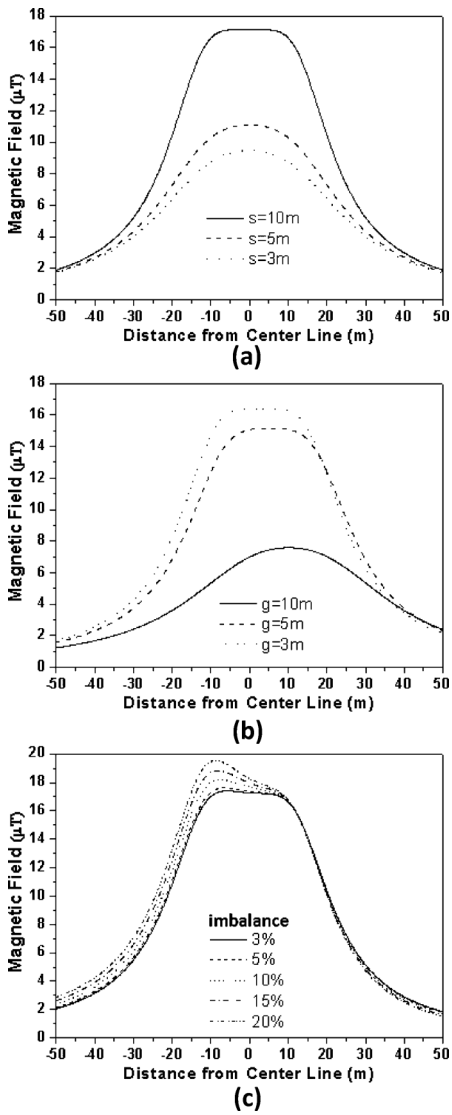

Fig. 4. Profile of the resulting magnetic field from the 500-kV transmission-line model in Fig. 3(a) at midspan. (a) Simulated with different sagging (s). (b) Simulated with different galloping (g). (c) Simulated with different current imbalance. The distance from the center line is along the x-direction.

of magnetic-field distribution at 1 m above the ground at the midspan.

Fig. 4 shows the magnetic-field distribution of the 500-kV transmission lines in Fig. 3(a). In Fig. 4(a), the magnetic field is simulated with different conductor sags. We assume that every conductor suffers the same sag. The magnetic-field distribution, in general, is the largest at the center line and decreases as it is farther away from the center line. With $\mathrm{s} = 3$ m, the maximum magnetic flux density of the resulting magnetic field is 9.5 μT. When the sag increases to 5 m, the maximum magnetic flux density rises to 11.0 μT. Finally, when the sag reaches 10 m, which is the maximum extent for safe operation, the maximum magnetic flux density is 17.2 μT. One can find that the conductor sagging does not exert any influence on the lateral position of the magnetic-field profile. When the lines are oscillating toward the x direction, the simulation results with different galloping (with the same sag of $\mathrm{s} = 10$ m) are shown in Fig. 4(b). We assume that every conductor suffers the same oscillation. As observed in the figure, when the galloping amplitude is 3 m, the profile of the magnetic field moves slightly toward the direction of the line oscillation, and the maximum field value decreases to 16.4 μT due to the increased height of phase conductors above the ground. Since the galloping amplitude increases to 5 m, the profile of field continues to depart from the center line and the maximum magnetic flux density reaches 15.2 μT. Finally, an extreme case of 10-m galloping is simulated. The maximum magnetic flux density decreases below 8 μT. The x-coordinate of the peak field value moves to $\mathrm{x} = 10$ m. These simulations demonstrate that the profile of the magnetic field is changed by the spatial variations of the transmission lines. As the transmission lines gallop sideways, the x-coordinate of the peak field value moves sideways correspondingly.

Apart from the spatial variation, current imbalance among phases also changes the magnetic-field distribution. The current imbalance, which is smaller than 3%, is considered as normal operation states. In order to study the influence of serious current imbalance on magnetic-field distribution, several possible situations are considered. The simulation results are shown in Fig. 4(c). For the 500-kV transmission lines [Fig. 3(a)], the current in phase B is greater than the rating value by 3%, 5%, 10%, 15%, and 20%, respectively. It can be observed that the magnetic-field profile is affected slightly by the current imbalance of 3% in phase B. Nevertheless, the change of the magnetic-field profile increases as the current imbalance is greater than 5%. When the 20% current imbalance occurs in phase B, the maximum magnetic flux density is obtained under the conductor of phase B and its value reaches approximately 20 μT.

The same simulations were carried out on the 220-kV double-circuit transmission-line model in Fig. 3(b). The simulation results are shown in Fig. 5. In Fig. 5(a), the amplitude of magnetic field rises when the sag increases from 4.78 to 6.78 m. In Fig. 5(b), the amplitude of magnetic field decreases with increasing line galloping, and the magnetic-field profile moves with the direction of the line oscillation (x-axis direction). In Fig. 5(c), the profile of the magnetic field changes significantly with an increasing percentage of current imbalance in the phase conductor. It should be noted that the current imbalance occurs in phase B in circuit 1 in Fig. 3(b).

The aforementioned simulation results show that different spatial and electrical variations of transmission lines result in corresponding changes of the magnetic-field distribution. Sagging changes the peak value of the magnetic-field profile, and it hardly affects the horizontal position of the peak field. Galloping changes the magnetic-field value and, at the same time, the field

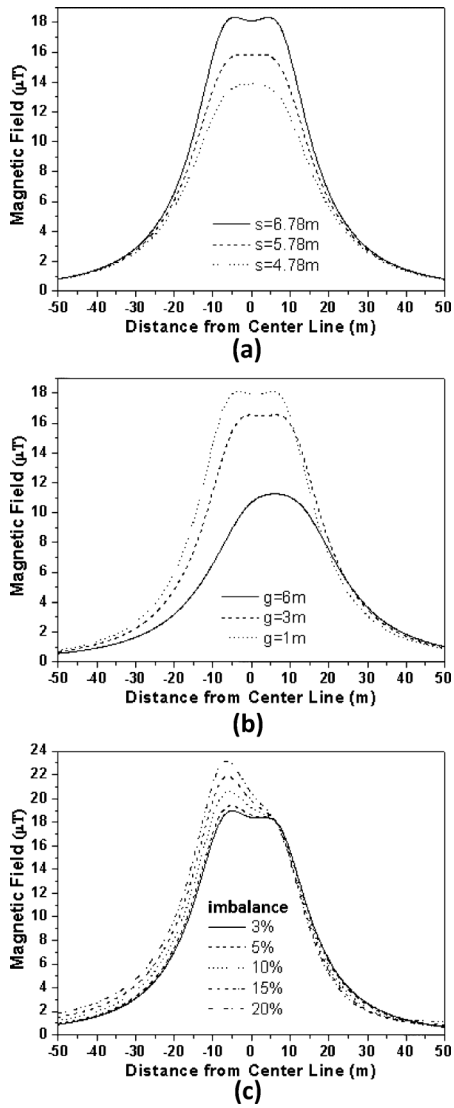

Fig. 5. Profile of the resulting magnetic field from the 220-kV double-circuit transmission-line model in Fig. 3(b) at midspan. (a) Simulated with different sagging (s). (b) Simulated with different galloping (g). (c) Simulated with different current imbalance.

profile moves with the galloping oscillation. In the case of current imbalance, the profile of the magnetic field is changed remarkably with a current imbalance greater than 5%. Especially, when the imbalanced phase is far away from the y-axis, the symmetry of the magnetic-field profile is broken and biased toward the imbalanced phase conductor. Under the imbalanced phase conductor, the magnetic flux density rises significantly.

III. Monitoring Technology Based on the Magnetic Field

Based on the correlation between the spatial and electrical parameters of transmission lines and the magnetic-field profile, an idea that one can estimate the transmission-line operation-state by measuring the emanated magnetic field was developed. The aforementioned simulation results show that: 1) conductor sagging is reflected in the rising amplitude of the magnetic-field profile; 2) transmission-line galloping changes the horizontal position of the magnetic-field profile; and 3) the profile shape

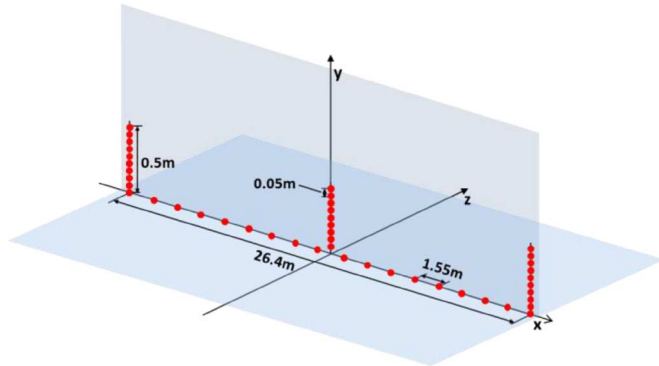

Fig. 6. Magnetic-field data-point distribution for magnetic-field simulation. The red dots denote the field points. In reality, the magnetic field value at each field point can be measured by an MR sensor.

is changed correspondingly when current imbalance occurs. It is therefore possible to develop a novel noncontact technology for transmission-line monitoring by magnetic-field sensing. The technology can provide the operation states of the transmission lines by measuring and processing the magnetic-field data collected at the ground level. It includes two important steps: 1) magnetic-field sensing, and 2) magnetic-field source reconstruction. This concept was implemented and verified experimentally on a scaled laboratory setup of transmission-line monitoring in our previous work with a single transmission line [10].

According to the simulations, the magnetic flux density at the ground level under a transmission line is typically on the order of 10^{-5} Tesla. Therefore, magnetic sensors with sufficient sensitivity should be provided. Size, spatial resolution, power consumption, as well as the cost of magnetic sensors should be considered. Presently, commercially available magnetoresistive (MR) sensors, including anisotropic magnetoresistance (AMR), giant magnetoresistance (GMR), and tunneling magnetoresistance (TMR) sensors, are able to sense the magnetic flux density from 10^{-7} to 10^{-9} Tesla, respectively [11]. Thus, MR sensors are sensitive enough to undertake the measurements of the transmission-line magnetic field. In addition, MR sensors are much smaller in size than traditional magnetic-field sensors, such as Hall sensors and fluxgates. This feature makes it possible to design a compact measurement system, which can sense the magnetic field with very high spatial resolution. An integrated power module of the measurement system can provide sufficient energy to the MR sensors since MR sensors have low-energy consumption and, thus, it is not necessary to obtain power from the transmission lines, avoiding the trouble of working on the live wires during installation. More important, such independence from the transmission system ensures that the monitoring systems based on MR sensors will still be functioning even if problems occur on the transmission system. In order to obtain a group of magnetic-field data points for source reconstruction, we calculate the magnetic field of 45 field points distributed in the x–y plane at the ground level under the transmission lines with the line configuration described in Fig. 3(a). The field point distribution is shown in Fig. 6. The field points denoted by the red dots are arranged in the form of vertical and horizontal arrays. Each of the three vertical arrays contains nine field points and is placed under each transmission-line cable for sensing the

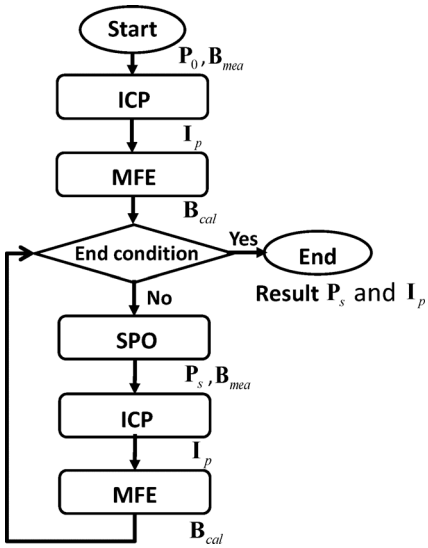

Fig. 7. Flowchart of current source reconstruction from magnetic-field sensing.

magnetic-field variation from each phase current. The interval of two neighbor points is 0.05 m. The horizontal array contains 18 field points and it is placed along the x-axis for measuring the wide-range magnetic field. There is a distance of 1.55 m between the neighboring field points. In reality, these field points can be measured by MR sensors.

With the measured magnetic-field data at these field points, defining the current sources of the magnetic field is required. In order to realize this, the stochastic optimization technique called the artificial immune system (AIS) algorithm is used to reconstruct the current sources from the magnetic-field data [10], [12]. This reconstruction process is described in the flowchart (Fig. 7). It starts with a group of default position parameters $\mathbf{P}_0$ of the transmission-line conductors, which are recorded under normal operation states. Phase currents $\mathbf{I}_p$ are calculated by an inverse current program (ICP), which is based on least-squares estimation, with position parameters and measured magnetic field $\mathbf{B}_{\rm mea}$ as variables by this equation

$$\mathbf{I}_p = (\mathbf{A}^{\rm T}\mathbf{A})^{-1}\mathbf{A}^{\rm T}\mathbf{B}_{\rm mea} \tag{1}$$

where $\mathbf{A}$ is the coefficient matrix which depends on the configuration of current sources. Then, the magnetic field $\mathbf{B}_{\rm cal}$ is obtained by using $\mathbf{I}_p$ and configuration parameters in the magnetic-field evaluation (MFE) module as

$$\mathbf{B}_{cal} = \mathbf{A}\mathbf{I}_p. \tag{2}$$

There is a predetermined minimum threshold value of the Euclidean distance $\|\mathbf{B}_{cal} - \mathbf{B}_{mea}\|$ as the end condition for terminating the optimizing process. If the $\mathbf{B}_{cal}$ generated by default position parameters does not satisfy the end condition, the algorithm will randomly generate new position parameters $\mathbf{P}_s$ by using the AIS algorithm in the source position optimization (SPO) module. With reference to the $\mathbf{B}_{mea}$ and the generated $\mathbf{P}_s$, each $\mathbf{I}_p$ is computed by ICP again. The $\mathbf{P}_s$ and new $\mathbf{I}_p$ are then used to calculate new $\mathbf{B}_{cal}$ in MFE. Then, the calculated $\mathbf{B}_{\rm cal}$ and $\mathbf{B}_{\rm mea}$ are compared again, and the Euclidean distance between them is found. When the Euclidean distance is within the minimum threshold value, the optimizing process is terminated, and then the resulting $\mathbf{P}_s$ and $\mathbf{I}_p$ are saved as the true values of transmission-line parameters; otherwise, the iteration continues. This reconstruction process is repeated multiple times (N) in order to obtain the final results of $\mathbf{P}_s$ which are the averages of these N optimizations. Accordingly, the final $\mathbf{I}_p$ is obtained from the optimized $\mathbf{P}_s$ and the measured magnetic field.

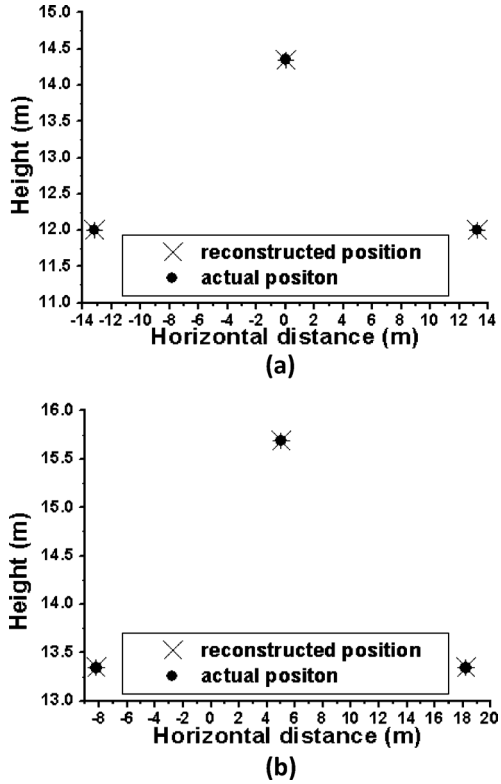

Fig. 8. Actual and reconstructed positions of phase conductors when (a) conductor sagging is 10 m, and (b) line galloping is 5 m with 10-m sag.

IV. Source Reconstruction Results

This reconstruction method was tested with the simulation model of a transmission-line system in four different scenarios ($N = 40$ in this case). Fig. 8 shows the reconstruction of the three-phase transmission-line configuration in Fig. 3(a) from the magnetic-field profile measured at the ground level. In the first scenario, the conductor positions are reconstructed from the magnetic field of the transmission lines when sagging of 10 m occurs as shown in Fig. 8(a). For the second scenario, Fig. 8(b) shows the reconstructed conductor positions with 5-m galloping and 10-m sagging. The average error between the reconstructed positions and the actual positions is less than 1 cm (0.1% of line-to-line distance). In these scenarios, the reconstruction method can locate the conductor positions accurately based on the measured magnetic-field data. Fig. 9 shows the reconstruction results of the third scenario that 10% current imbalance occurs in phase B. The reconstructed positions match the actual positions well with an error of less than 1 cm [Fig. 9(a)]. The reconstruction was repeated every 1 ms during a phase current cycle (20 ms for the 50-Hz system), and the

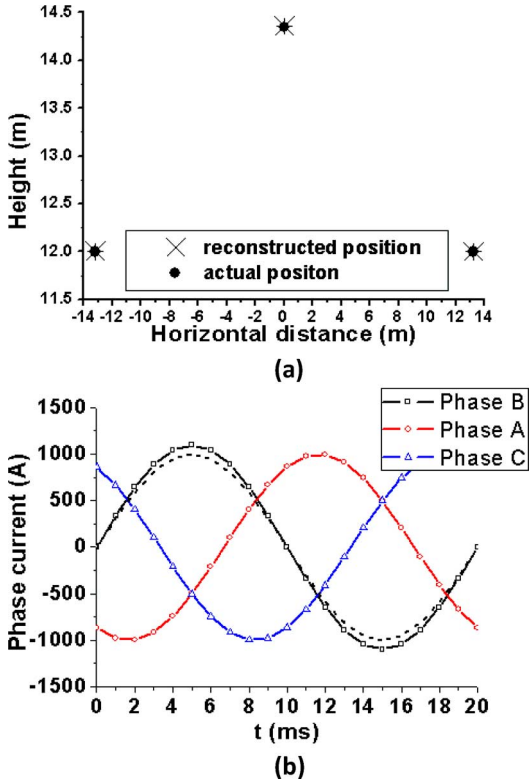

Fig. 9. Results of current source reconstruction when +10% current imbalance occurs in phase B of Fig. 3(a): (a) actual and reconstructed positions of the phase conductors and (b) phase current curve of each phase conductor. The dashed line denotes the current curve when no current imbalance occurs in phase B.

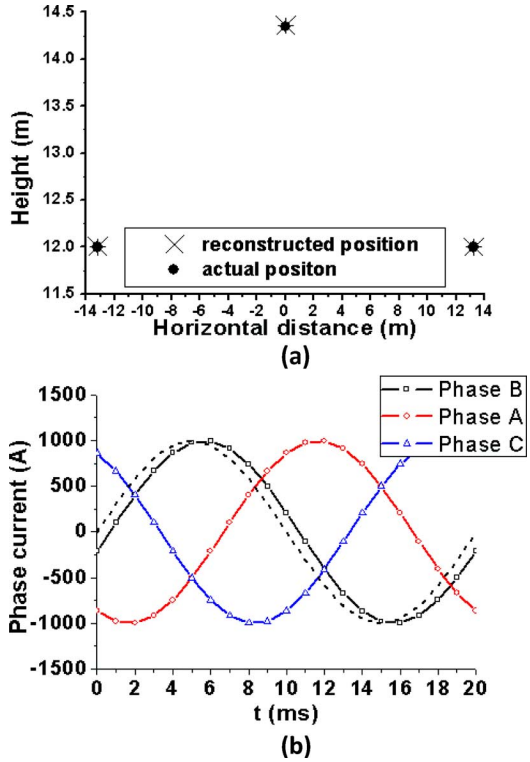

Fig. 10. Results of current source reconstruction when +10% current phase imbalance occurs in phase B of Fig. 3(a): (a) actual and reconstructed positions of phase conductors and (b) phase current curve of each phase conductor. The dashed line denotes the current curve when no current imbalance occurs in phase B.

complete phase current curves for the three phases can be obtained. Fig. 9(b) shows that each reconstructed phase current matches well with the actual phase current, and the 10% current amplitude imbalance (actual current amplitude is 1100 A) in phase B is also accurately deduced. In Fig. 10, the reconstruction results are shown for the fourth scenario where there is 10% imbalance in the phase angle (the phase angle changes from 0° to −12°) of phase B. From Fig. 10(a), the actual conductor positions are found with the error (1 cm) of less than 0.1% of line-to-line distance. By repeating the reconstruction every 1 ms throughout 20 ms, the complete phase current curves for the three phases are obtained in Fig. 10(b). It is found that each reconstructed phase current matches well with the actual phase current. The 10% phase imbalance in phase B is accurately reflected by the 0.67-ms delay of the phase B current curve along the time-axis which is equivalent to −12.06° in the phase angle. We can extract the information of frequency from the phase current curves in Fig. 9(b) and Fig. 10(b). By determining the periods of the phase current cycles from these curves, the current cycles are found to be 19.85 and 19.98 ms, respectively. As a result, we can deduce the system frequencies to be 50.38 Hz and 50.05 Hz for these two scenarios. The errors of the deduced frequencies are 0.38 Hz and 0.05 Hz, respectively, which are less than 1%. To summarize, the reconstructed results for the four scenarios—sagging, galloping, and current imbalance (amplitude and phase)—are provided. The reconstructed spatial values Q_{rec} of these four scenarios are compared with the actual value Q_{act} as shown in Table I. It indicates that for each

TABLE I
ACTUAL AND RECONSTRUCTED POSITIONS OF THE PHASE CONDUCTORS

		Phase B position (x, y) (m)	Phase A position (x, y) (m)	Phase C position (x, y) (m)
1st	Q_{act}	(-13.2, 12.0)	(0, 14.35)	(13.2, 12.0)
	Q_{rec}	(-13.194, 12.004)	(0.0054, 14.348)	(13.201, 12.003)
2nd	Q_{act}	(-8.2, 13.34)	(5.0, 15.69)	(18.2, 13.34)
	Q_{rec}	(-8.202, 13.345)	(5.004, 15.692)	(18.2, 13.343)
3rd	Q_{act}	(-13.2, 12.0)	(0, 14.35)	(13.2, 12.0)
	Q_{rec}	(-13.203, 12.0)	(-0.002, 14.358)	(13.199, 11.996)
4th	Q_{act}	(-13.2, 12.0)	(0, 14.35)	(13.2, 12.0)
	Q_{rec}	(-13.201, 12.0)	(0, 14.355)	(13.206, 11.999)

scenario, the method provides the accurate locations of conductors with an error of less than 1 cm. The values of current amplitude and phase angle are compared in Table II. For the first and second scenarios, phase currents were reconstructed with an average error of 0.2 A in amplitude and 0.02° in phase angle. For the third scenario where current amplitude imbalance occurs in phase B, the amplitude of phase B is found to be 1100.1 A which is very close to the actual value of 1100 A. The initial angle of each phase is reconstructed with an error of less than 0.03°. In the fourth scenario, the phase imbalance in phase B is found to be −11.99°, which is approximately equal to the actual value of −12°.

This method was repeated with the 220-kV double-circuit transmission-line model in Fig. 3(b). Four scenarios—sagging

TABLE II
ACTUAL AND RECONSTRUCTED PARAMETERS OF THE PHASE CURRENT

		Amplitude I_B, I_A, I_C (A)	Phase angle ϕ_B, ϕ_A, ϕ_C
1st	Q_{act}	1000, 1000, 1000	$0^\circ, -120^\circ, 120^\circ$
	Q_{rec}	1000.3, 1000.2, 1000.1	$-0.02^\circ, -120.04^\circ, 119.98^\circ$
2nd	Q_{act}	1000, 1000, 1000	$0^\circ, -120^\circ, 120^\circ$
	Q_{rec}	1000.0, 999.9, 1000.2	$0.01^\circ, -120.0^\circ, 119.99^\circ$
3rd	Q_{act}	1100, 1000, 1000	$0^\circ, -120^\circ, 120^\circ$
	Q_{rec}	1100.1, 1000.6, 1000.2	$0.03^\circ, -119.98^\circ, 119.99^\circ$
4th	Q_{act}	1000, 1000, 1000	$-12^\circ, -120^\circ, 120^\circ$
	Q_{rec}	1000.1, 1000.1, 999.8	$-11.99^\circ, -120.03^\circ, 119.99^\circ$

of 6.78 m, galloping of 6.0 m, and +10% current imbalance (phase B of circuit 1) in amplitude and phase angle were tested, respectively. For the spatial parameters, the conductor positions of the double circuit are located with an error of less than 0.2% of the line-to-line distance. The phase currents were reconstructed with an average error of 0.3 A in amplitude and 0.03° in phase angle. Again, the reconstructed results are very close to the actual values.

V. CONCLUSION

A novel noncontact technology of operation-state monitoring for an HV transmission line was proposed and demonstrated in this paper. Efforts were made to develop this technology to overcome the shortcomings of existing methods, such as inaccuracy, contact operation mode, installation with live wire, high-cost, instability, and single function. This paper studied the variation of the magnetic field emanated from overhead power transmission lines under different transmission-line operation states. The simulation results show that the magnetic-field distribution reflects the operation-state changes in the transmission-line spatial and electrical configurations. Interferences from ambient conditions, such as rough weather conditions, can be totally avoided. The source reconstruction method was proposed to reconstruct the position parameters and phase current of the transmission lines from the magnetic field measured by MR sensors. It enables simultaneous monitoring of electrical and spatial parameters of the transmission lines with high accuracy. When a group of magnetic-field data is measured and processed, the information of all line conductors within a span can be obtained. Moreover, thanks to its noncontact characteristic, additional online equipment are not required and installation and maintenance works on live wires are avoided. Thus, the technology is simple and low cost, which can be applied in large scale and to realize wide-area monitoring of transmission lines in the future smart grid.

APPENDIX

To apply the Biot–Savart law in calculating the magnetic field of overhead transmission lines, the following approximations are adopted to simplify the calculation:

1) the contributions of the currents in the vicinity of transmission lines are ignored; for example, the induced currents in transmission towers are not considered as field sources;
2) the magnetic field created by neighboring span lines is not taken into account;
3) the effect of harmonic currents is ignored;
4) the model involving double circuits is included in this work, but phase shift effects between them are not discussed here.

Even though errors may be incurred by the aforementioned approximations, the method can still provide calculation results similar to the measured magnetic-field values.

The magnetic field generated by a conductor carrying current I_i can be determined by using the Biot-Savart law

$$\mathbf{B}_i = \frac{\mu_0}{4\pi} \int \frac{I_i d\mathbf{l} \times \mathbf{r}}{|r|^3} \tag{3}$$

where $\mathbf{B}_i$ is magnetic flux density at the field point, μ_0 is the magnetic permeability of free space, I_i is the current flowing in the ith conductor of the transmission line within the span ($i = 1, 2, \ldots N$), $d\mathbf{l}$ is the element vector of source at the direction of the current, and $\mathbf{r}$ is the displacement vector from the source element to the field point. When taking other cable sources into account within the same span, the resulting magnetic field can be determined by applying the principle of superposition as

$$\mathbf{B} = \sum_{i=1}^{N} \mathbf{B}_i. \tag{4}$$

By the same token, the magnetic field generated by the image currents can be superimposed upon that generated by the transmission-line conductors. The image methodology was used to calculate the contribution of the image current source in the conducting ground [13]. The image current is located at a depth of $h + \alpha$ in the opposite direction, where h is the height of the real current element from the ground, and α is the complex depth of the image current element given by

$$\alpha = \sqrt{2}\delta e^{-j\pi/4}. \tag{5}$$

The parameter δ denotes the skin depth of earth as given

$$\delta = \sqrt{\rho/\pi\mu f} \tag{6}$$

where ρ is the resistivity of the earth, μ is the magnetic permeability of the earth, and f is the source current frequency in Hz (50 Hz in this work). $\rho = 100\ \Omega$ is chosen here to calculate the complex distance α. Now, we can provide the vector expressions of the resulting magnetic field generated by a straight conductor carrying current and its image current

$$\begin{aligned} B_{i,x} &= \frac{\mu_0 I_i}{2\pi}\left(-\frac{y-y_i}{(x-x_i)^2+(y-y_i)^2} + \frac{y+y_i+\alpha}{(x-x_i)^2+(y-y_i+\alpha)^2}\right) \\ B_{i,y} &= \frac{\mu_0 I_i}{2\pi}\left(-\frac{x-x_i}{(x-x_i)^2+(y-y_i)^2} + \frac{x-x_i}{(x-x_i)^2+(y-y_i+\alpha)^2}\right) \\ B_{i,z} &= 0. \end{aligned} \tag{7}$$

For the scenario of conductor sagging, the equation of the conductor catenary is given by

$$y = a\cosh\left(\frac{z}{a}\right) + y_0 \tag{8}$$

where a and y_0 are determined by the origin of the catenary coordinate system [14]. Its differential vector element can be written as

$$d\mathbf{l} = \mathbf{sinh}\left(\frac{z}{a}\right)dz\mathbf{a}_y + dz\mathbf{a}_z. \tag{9}$$

By applying the Biot–Savart law and considering the effect of catenary, the total magnetic field generated by a sagging conductor at the field point is given by

$$\begin{aligned}
B_{i,x} &= \frac{\mu_0 I_i}{4\pi}\int_{-L/2}^{L/2}\frac{\sinh(z_i/a)(z-z_i)-(y-y_i)}{[(x-x_i)^2+(y-y_i)^2+(z-z_i)^2]^{3/2}}dz_i \\
B_{i,y} &= \frac{\mu_0 I_i}{4\pi}\int_{-L/2}^{L/2}\frac{(x-x_i)}{[(x-x_i)^2+(y-y_i)^2+(z-z_i)^2]^{3/2}}dz_i \\
B_{i,z} &= \frac{\mu_0 I_i}{4\pi}\int_{-L/2}^{L/2}\frac{-\sinh(z_i/a)(x-x_i)}{[(x-x_i)^2+(y-y_i)^2+(z-z_i)^2]^{3/2}}dz_i.
\end{aligned} \tag{10}$$

For the scenario of transmission-line galloping, as shown in Fig. 2, the original coordinate system is rotated to keep the galloping conductor in the same plane as the $S_\perp$ plane so that the emanated magnetic field from the galloping conductor can be calculated by the same equations in (10). The coordinate values of the field points are modified according to the rotated coordinate system. Since the conductor actually moves farther from the ground when it is galloping, the effect of the image current on the magnetic field is even weaker. It is calculated to be less than 0.002 μTesla in our case which is more than 1000 times smaller than the typical emanated magnetic field from the overhead transmission lines. As such, the image current is not taken into account in the case of galloping in order to ease the computation.

REFERENCES

[1] V. Terzija, G. Valerde, D. Cai, P. Regulski, V. Mandani, J. Fitch, S. Skok, M. Begovic, and A. Phadke, "Wide-area monitoring, protection, and control of future electric power networks," *Proc. IEEE*, vol. 99, no. 1, pp. 80–93, Jan. 2011.

[2] A. Cataliotti, D. Cara, A. E. Emanuel, and S. Nuccio, "Characterization of current transformers in the presence of Harmonic distortion," presented at the IMTC IEEE Int. Instrum. Meas. Technol. Conf., Victoria, BC, Canada, 2008.

[3] A. Cataliotti, D. Cara, P. A. Franco, A. E. Emanuel, and S. Nuccio, "Frequency response of measurement current transformers," presented at the IMTC IEEE Int. Instrum. Meas. Technol. Conf., Victoria, BC, Canada, 2008.

[4] Arteche Group, Jun. 11, 2013. [Online]. Available: http://www.arteche.com/

[5] The Valley Group, Tension monitor, Feb. 05, 2010. [Online]. Available: http://www.cat-1.com

[6] Siemens AG, Mar. 18, 2013. [Online]. Available: www.automation.siemens.com

[7] C. Mensah-Bonsu, U. F. Krekeler, G. T. Heydt, Y. Hoverson, J. Schilleci, and B. L. Agrawal, "Application of the global positioning system to the measurement of overhead power transmission conductor sag," *IEEE Trans. Power Del.*, vol. 17, no. 1, pp. 273–278, Jan. 2002.

[8] Western Area Power Administration, "Transmission enhancement technology report," Billings, MT, USA, 2002.

[9] L. Fish, "Low cost sensors for real time monitoring of overhead transmission lines," Washington, DC, USA, Rep. no. 79057S05-I, 2006.

[10] X. Sun, K. S. Lui, K. K. Y. Wong, W. K. Lee, Y. Hou, Q. Huang, and P. W. T. Pong, "Novel application of magnetoresistive sensors for high-voltage transmission-line monitoring," *IEEE Trans. Magn.*, vol. 47, no. 10, pp. 2608–2611, Oct. 2011.

[11] NVE Corp., May 06, 2011. [Online]. Available: http://www.nve.com

[12] P. Neittaanmaki, M. Rudnicki, and A. Savini, *Inverse Problems and Optimal Design in Electricity and Magnetism*. New York: Oxford University Press Inc., 1996.

[13] K. Budnik and W. Machczynski, "Contribution to studies on calculation of the magnetic field under power lines," *Eur. Trans. Elect. Power*, vol. 16, pp. 345–364, Jul./Aug. 2006.

[14] A. V. Mamishev, R. D. Nevels, and B. D. Russell, "Effects of conductor sag on spatial distribution of power line magnetic field," *IEEE Tran. Power Del.*, vol. 11, no. 3, pp. 1571–1576, Jul. 1996.

Xu Sun received the B.S. degree in electronic information engineering from the Northeast China Institute of Electric Power (NEIEP), Jilin, China, in 2005, the M.S. degree in physical electronics from the University of Electronic Science and Technology of China (UESTC), Chengdu, China, in 2008, and is currently pursuing the Ph.D. degree in electrical and electronic engineering (EEE) at the University of Hong Kong (HKU).

His research interests focus on electromagnetics, computational electromagnetics, stochastic optimization, application of magnetoresistive (MR) sensors in power systems, and electric power transmission monitoring.

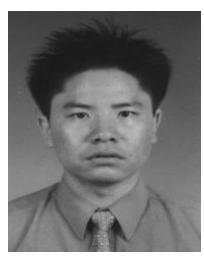

Qi Huang (S'99–M'03–SM'09) received the B.S. degree in electrical engineering from Fuzhou University, Fuzhou, China, in 1996, the M.S. degree in electrical engineering from Tsinghua University, Beijing, China, in 1999, and the Ph.D. degree in electrical engineering from Arizona State University, Tempe, AZ, USA, in 2003.

Currently, he is a Professor at University of Electronic Science and Technology of China (UESTC) and the Deputy Dean of School of Energy Science and Engineering, UESTC, and the Director of Sichuan State Provincial Lab of Power System Wide-Area Measurement and Control, Chengdu, Sichuan, China. His current research and academic interests include power system high-performance computing, power system instrumentation, power system monitoring and control, and integration of distributed generation into the existing power system infrastructure.

Yunhe Hou (M'06) received the B.E. and Ph.D. degrees in electrical engineering from Huazhong University of Science and Technology, Wuhan, China, in 1999 and 2005, respectively.

He was a Postdoctoral Researcher at Tsinghua University, Beijing, China; Iowa State University, Ames, IA, USA; University College Dublin, Ireland; and Massachusetts Institute of Technology, Cambridge, MA, USA. Currently, he is with the University of Hong Kong, Hong Kong, China, as an Assistant Professor. He is also a Guest Professor with the State Key Laboratory of Advanced Electromagnetic Engineering and Technology of China, Wuhan.

Lijun Jiang (S'01–M'04–SM'13) received the B.S. degree in electrical engineering from the Beijing University of Aeronautics and Astronautics, Beijing, China, in 1993, the M.S. degree in electrical engineering from Tsinghua University, Beijing, China, in 1996, and the Ph.D. degree in electromagnetics from the University of Illinois at Urbana-Champaign, IL, USA, in 2004.

Since 2004, he has been the Postdoctoral Researcher, the Research Staff Member, and the Senior Engineer at IBM T. J. Watson Research Center, Yorktown Heights, NY, USA. Since the end of 2009, he has been an Associate Professor with EEE at the University of Hong Kong, Hong Kong, China. His research interests focus on electromagnetics, computational electromagnetics, integrated-circuit (IC) signal/power integrity, IC electromagnetic-compatibility/electromagnetic-interference antennas, multidisciplinary electronic-design-automation solutions, RF and microwave technologies, high–performance computing (HPC), etc.

Philip W. T. Pong (SM'13) received the Ph.D. degree in engineering from the University of Cambridge, Cambridge, U.K., in 2005.

Currently, he is a Physicist and Electrical Engineer, working on magnetoresistive magnetic-field sensors and smart grid in the Department of Electrical and Electronic Engineering (EEE), the University of Hong Kong (HKU), Hong Kong, China.

He was a Postdoctoral Researcher at the Magnetic Materials Group, National Institute of Standards and Technology (NIST), Gaithersburg, MD, USA, for three years. In 2008, he joined the HKU engineering faculty as an Assistant Professor, working on tunneling magnetoresistance (TMR) sensors, and the application of magnetoresistive sensors in smart grid.